Breathing mode in Hall effect thrusters

IEPC-2015-283／ISTS-2015-b-283

Presented at Joint Conference of 30th International Symposium on Space Technology and Science,
34th International Electric Propulsion Conference and 6th Nano-satellite Symposium
Hyogo-Kobe, Japan
July 4–10, 2015

Kentaro Hara*and Iain D. Boyd†
University of Michigan, Ann Arbor, MI, 48109, USA

Michael J. Sekerak‡
Jet Propulsion Laboratory, California Institute of Technology, Pasadena, CA 91109

and

Alec D. Gallimore§
University of Michigan, Ann Arbor, MI, 48109, USA

The mechanism of breathing mode oscillations in Hall effect thrusters is discussed using a hybrid-direct kinetic simulation [Hara et al. J. Appl. Phys. 115, 203304 (2014)] and a perturbation theory of ionization oscillations [Hara et al. Phys. Plasmas 21, 122103 (2014)]. The results obtained from the simulations suggest that mode transition of the discharge oscillations occurs due to electron transport. Although the common understanding is that insufficient neutral atom flow is the main contributor to the breathing mode, this is not likely the cause of the oscillations since stabilization of discharge oscillations is observed during a constant anode mass flow. Changes in the electron temperature and electron axial mean velocity are observed from the hybrid-DK simulation when the magnetic field strength is varied. In addition, a linear perturbation theory of ionization oscillations is developed to investigate the direct cause of the stabilization and excitation of breathing mode oscillations. Ionization instability is unconditionally stable when the ion and neutral atom transport equations are only taken into consideration as the fixed anode mass flow can damp any low-frequency oscillation. A linearly unstable mode is observed only when the perturbation of electron energy is included. It was observed from both the numerical simulation and perturbation theory that a large wall heat flux damps ionization oscillations while a large convective heat flux contributes to excitation of the oscillations.

I. Introduction

THE breathing mode has been observed in Hall effect thrusters (HETs) in several numerical studies[1,2,3,4] and experiments[5,6,7] but differences between the oscillation modes have not been discussed. Although several theoretical frameworks have been developed,[2,4,8] no complete theoretical justification and explanation of the discharge and plasma oscillations have been made.

In this paper, the stabilization and excitation of breathing mode oscillations are discussed using computer simulation and a perturbation theory. The first half of this paper discusses the mode transition of discharge oscillations in HETs using an improved version of the 1D hybrid-DK simulation presented in Ref. 9. This

*Postdoctoral Research Fellow, Department of Aerospace Engineering, University of Michigan, kenhara@umich.edu
†Professor, Department of Aerospace Engineering, University of Michigan, iainboyd@umich.edu
‡Engineer, Electric Propulsion Group, 4800 Oak Grove Dr., MS 125-109, Pasadena, CA, 91109, michael.j.sekerak@jpl.nasa.gov
§Professor, Department of Aerospace Engineering, University of Michigan, alec.gallimore@umich.edu

model includes an improved electron fluid model as well as ground- and excited-state neutral atom transport models in addition to the hybrid model presented in Refs. 10 and 11 . The second half includes the perturbation theory proposed in Ref. 12. The predator-prey model is revisited and a perturbation theory including the electron temperature equation is developed.

II. Mode transition study using a hybrid-DK simulation

The discharge plasma of a SPT-100 Hall thruster is modeled using a 1D hybrid-DK simulation. A DK simulation is used for ions, a fluid model which solves the momentum and energy equations is used for electrons, and neutral atoms are modeled solving the continuity equation. The numerical method and results are presented in Ref. 9 in detail.

A. Computational Method

The configuration is identical to the SPT-100ML thrusters.[3,6] The calculation domain is taken from $x = 0$ cm, the anode, to $x = 3.5$ cm, which is assumed to be the cathode line where the electron total energy is chosen as 10 eV and the potential is 0 V. The channel length is 2.5 cm. The discharge voltage is 300 V, anode mass flow rate is 5.0 mg/s, and the peak magnetic field is varied. Background pressure is not accounted for in the present model and charge exchange collisions are neglected.

The 1D transport equation for the ions is given by

$$\frac{\partial f}{\partial t} + v_x \frac{\partial f}{\partial x} + \frac{eE}{M} \frac{\partial f}{\partial v_x} = S \tag{1}$$

where E is the electric field, e is the elementary charge, M is the ion mass, f and S are the VDF and the collision term respectively, which are functions of the axial position, x, the axial velocity v_x, and time t. Macroscopic quantities, such as number density and mean velocity, are obtained by calculating the moments of the VDFs. The source term for ions include singly charged ionization in this model.

The transport of ground-state and electronically excited atoms are modeled by solving the continuity equation.

$$\frac{\partial n_n}{\partial t} + \frac{\partial}{\partial x}(n_n u_n) = \sum_{\text{reactions}} \dot{n}_n, \tag{2}$$

where $\dot{n}_n$ is the source term due to collisional reactions. The axial neutral atom velocity is assumed to be constant: $u_n = 250$ m/s. For the ground-state neutral atoms, electron-impact excitation, electron-impact ionization, and wall diffusion are taken into consideration. For the excited-state neutral atoms, electron-impact excitation, and electron-impact stepwise ionization are included in the model.

The 1D electron momentum equation is written as

$$v_{ex} = -\mu_{eff} \left[E_x + \frac{1}{n_e} \frac{\partial}{\partial x} (n_e T_e) \right] \tag{3}$$

where μ_{eff} is the effective electron mobility and v_{ex} is the axial electron drift velocity which is obtained from current conservation. The effective electron mobility is determined by the magnetic field and effective momentum transfer collision frequency, ν_{eff}, that is described as the sum of electron-neutral elastic collisions, electron-impact inelastic collisions, electron-wall collisions, Coulomb collisions, and any contributions from anomalous transport. The values and models used are described in Ref. 9. Coulomb collisions are found to be unimportant under the plasma parameters in the Hall thruster discharge.

The electron energy equation is described by the balance between convective heat flux, Joule heating, wall losses, and inelastic collisions.[13]

$$\frac{\partial}{\partial x} \left(\frac{5}{3} n v_{ex} \varepsilon \right) = n_e v_{ex} E_\perp - n_e \left[\nu_{ew} \Delta\varepsilon_w + \sum_j \nu_j \Delta\varepsilon_j \right] \tag{4}$$

where ε is the mean electron energy, ν_{ew} is the electron-wall collision frequency, $\Delta\varepsilon_w$ is the energy loss to the wall, ν_j is the collision frequency and $\Delta\varepsilon_j$ is the energy loss due to an inelastic collision, j. The mean electron energy can be decomposed into

$$\varepsilon = \frac{3}{2} T_{eV} + K_{eV} \tag{5}$$

where T_{eV} is the electron temperature in electron-volts, $K_{eV} = \frac{1}{2}m_e(v_{ex}^2 + v_{e\theta}^2)/e$ is the kinetic energy in electron-volts, and $v_{e\theta} = v_{ex}\Omega$ is the azimuthal velocity.

B. Flowchart

Figure 1 shows the flowchart of the hybrid-DK simulation.

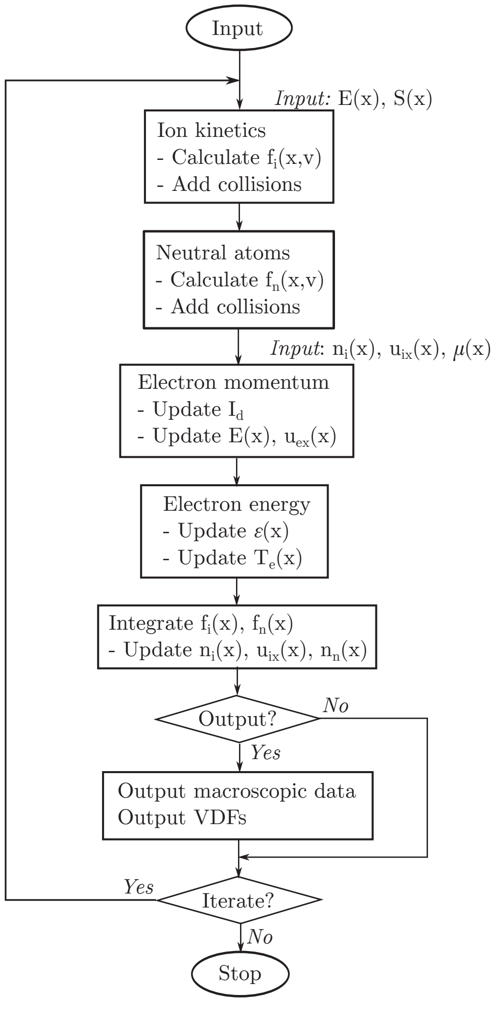

Figure 1. Flowchart of the hybrid model for HET discharge plasmas.

First, the ion and neutral atom kinetic solvers are called. Here, the input parameters for the ion kinetic solver are the electric field and the collision terms on the right hand side of the kinetic equation. For the neutral atom solver, only the collision terms are needed.

Next, the electron continuum module is called. The discharge current is calculated first from the charge conservation equation along with the drift-diffusion approximation for the electron momentum equation. Inputs for this module are the ion number density, ion flux (or the mean velocity), and the electron mobility. Once the discharge current is calculated, the electric field is calculated. The electron mean velocity can then also be calculated from the current conservation. The steady-state electron energy equation is solved to obtain the electron mean energy, ε. In this study, the azimuthal electron drift is neglected so the electron temperature in electron-volts is simply $T_e = (2/3)\varepsilon$.

Finally, the ion and neutral atom VDFs obtained from the kinetic solver are integrated to update the number densities and the velocities. This integration process must be performed after the electron module so that the input for the electron module is the information at the old time step.

The time step of the simulation is chosen to be 1 ns. Data output is performed typically every 500 time steps, *i.e.* 500 ns. The simulation stops when the simulation time is 1 ms. Therefore, the hybrid model is iterated for 10^6 time steps.

III. Mode Transition Results

Mode transition of the discharge plasma oscillations is studied comparing the hybrid-DK simulation of an SPT-100 thruster to experiments of the H6 thruster.

A. Comparison with Experiments

Figure 2 shows the discharge current oscillations in both the H6 experiment and the SPT-100 simulation. Figures 2(a) and 2(b) show the H6 experiments and correspond to $B_r/B_r^* = 0.52$ and 0.61, where B_r^* is the maximum magnetic field strength. On the other hand, Figs. 2(c) and 2(d) correspond to simulation results at $B = 120$ G and 180 G, respectively.

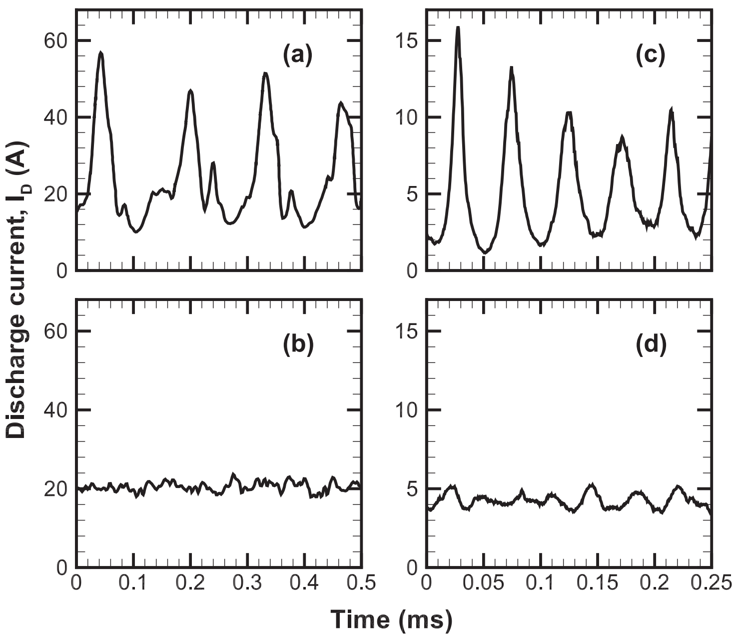

Figure 2. Discharge current oscillation: (a) $B_r/B_r^* = 0.52$ (H6), (b) $B_r/B_r^* = 0.61$ (H6), (c) B=120 G (Hybrid-DK), (d) B=180 G (Hybrid-DK). Reproduced from Ref. 9.

The shape of the discharge current oscillation exhibits excellent agreement between the two data sets. The oscillation mode is a non-sinusoidal oscillation in which the maximum current is almost three times larger than the mean discharge current. In the stable mode, the discharge current is not completely stationary but exhibits a small amplitude oscillation that is a superposition of several modes. Note that there is high frequency noise present in some regions during the breathing mode oscillation in the numerical results. These oscillations come from the pressure gradient in the electron continuum model as the first derivative of the product of the number density and the electron temperature is taken and the electric field is calculated. This may be numerical but can also be physical in that the pressure gradient can cause acoustic type waves in the system.

Figure 3 shows the frequency of the discharge current oscillations obtained in the breathing mode from the H6 experiment and the SPT-100 simulation. The frequencies in Fig. 3(a) are determined by fitting a Lorentzian to the discharge current power spectral density in order to identify the peak frequency. An agreement of the trend between the experimental data and the simulation results is shown although the magnitude of the frequency does not agree due to the difference in the thruster geometry and operational point. Note that the breathing mode frequency of 20 - 25 kHz from the SPT-100 simulation agrees with the previous experiment by Gascon *et al.*[6]

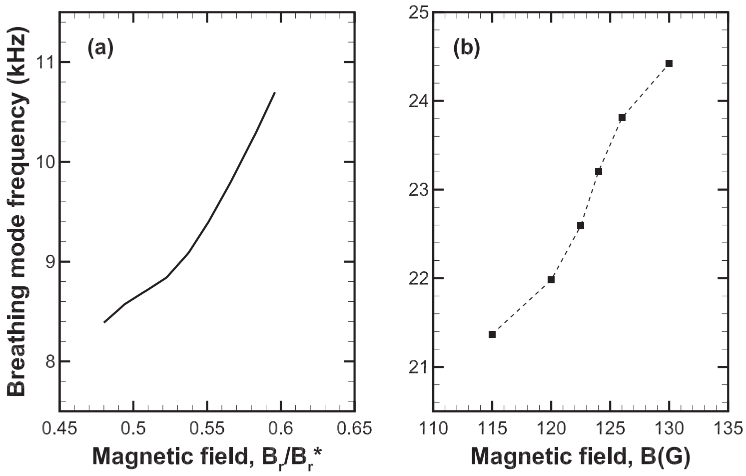

Figure 3. Breathing mode frequency: (a) H6 experiment,[14] (b) SPT-100 simulation. Reproduced from Ref. 9.

B. Electron Energy Balance

Although the breathing mode oscillation is a low-frequency oscillation that results in the transport of slow neutral atoms interacting with ions and electrons, the ionization oscillation is strongly associated with the electron transport and hence the electron energy.

Figure 4 shows the spatial distributions of the time-averaged kinetic and thermal energy for two different thruster operating modes. In both modes, the electron kinetic energy is largest near the channel exit inside the channel where the $E \times B$ drift is strongest. As the electric field weakens inside the channel, the electron kinetic energy due to the azimuthal drift decreases. The time-averaged electron temperature is below 25 eV, which is the critical electron temperature.

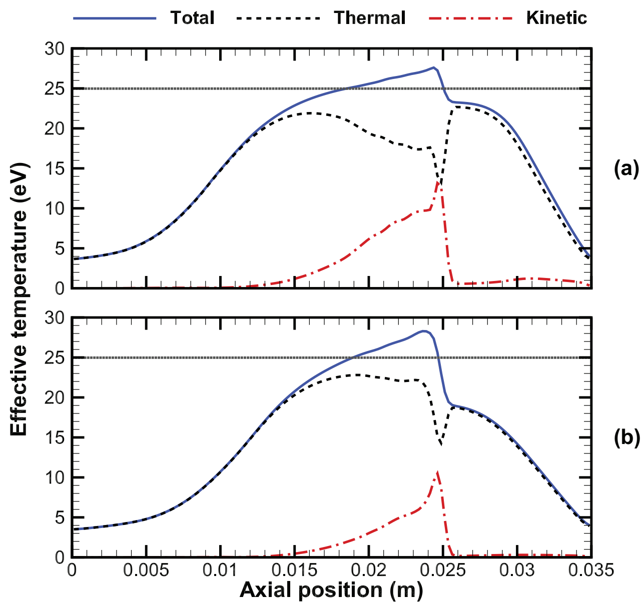

Figure 4. Time-averaged kinetic energy and thermal energy components. Horizontal dotted line is the critical electron temperature that forms a SCL sheath: (a) Oscillatory mode B=120 G; (b) Stable mode B=180 G. Reproduced from Ref. 9.

The spatial distribution of the time-averaged energy contributions in the two operation modes are shown in Fig. 5. As all contributions are almost identical near the anode (*i.e.* $x < 0.012$ m) and in the plume (*i.e.* $x > 0.025$ m), it can be considered that the breathing mode is either excited or stabilized mainly due to the ionization and acceleration regions in the discharge channel near the channel exit. In the oscillatory mode (B = 120 G), the convective heat flux, which is the energy transfer due to the electron axial velocity, is large and balances the Joule heating while the wall heat flux is small due to the low electron thermal energy shown. The electrons are poorly confined and plasma oscillation occurs. In the stable mode (B = 180 G), the electron axial drift is reduced and the convective heat flux decreases as the magnetic field strength increases. The wall heat flux balances the Joule heating. The plasma-wall interaction plays an important role due to the increase in the electron thermal energy, as shown in Fig. 4. It is therefore suggested that the stabilization of discharge oscillation is associated with the balance between energy gain and loss and that there is an axial electron drift required for a stable operation mode.

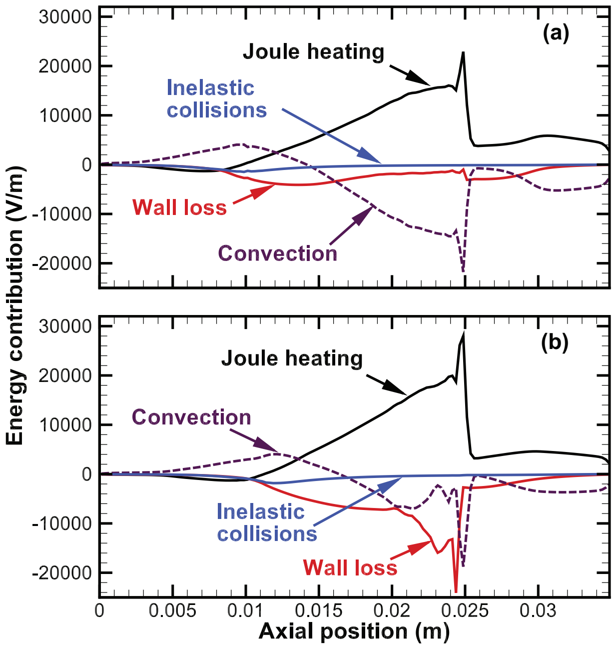

Figure 5. Time-averaged electron energy transfer. Each term in Eq. (4) is divided by the electron axial current.: (a) Oscillatory mode B=120 G; (b) Stable mode B=180 G. Reproduced from Ref. 9.

C. Electron Transport

Figure 6 shows the time-averaged axial electron velocities for the two oscillation modes. Electron velocities in the axial direction are negative because the electrons drift from the cathode to the anode. If the electron temperature at the plume is constant in the two modes, the electron energy inflow into the discharge channel from the plume is larger as the electron axial velocity increases negatively. At the stable mode (B = 180 G), the electron axial velocity is reduced in the plume so that the convective heat flux into the discharge channel decreases. Note that electron axial velocity is on the order of 0.001 eV, thus the axial component of the electron drift is negligible in the kinetic energy.

IV. Theory: Only including ion and neutral atom transport

The mechanism of ionization oscillations in HETs has been explained by insufficient neutral flow for decades.[1,2,15] Previous theories have been formulated using the transport of heavy species, *i.e.* neutral atoms and ions. In the HET community, the predator-prey model,[2] of which the simplest form is also known as the Lotka-Volterra model, has been widely used.

In the low temperature plasma community, a global model is often used to calculate the number densities of all chemical species.[16] Such models account for chemical reactions and some of the important physical phenomena, including diffusion, gas flow, and power input. In this section, a framework similar to global

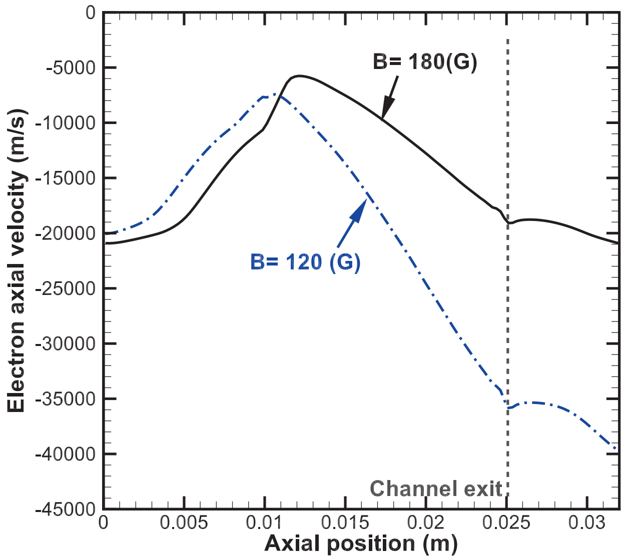

Figure 6. Time-averaged axial electron velocity. Reproduced from Ref. 9.

models is constructed to perform a perturbation analysis to investigate the excitation and stabilization of ionization oscillations in HETs. The detail of the theory is presented in Ref. 12.

A. Predator-prey model

The predator-prey model assumes that the plasma is contained in an ionization box whose length is L and the spatial variation is neglected. The ionization rate coefficient ξ_{ion} and the velocities of ions and neutral atoms are constant in time. There is no ion flux entering the box and no neutral flux escaping the box. Using these assumptions, the continuity equations are written as

$$\frac{\partial N_i}{\partial t} + \frac{N_i U_i}{L} = N_i N_n \xi_{ion} \quad (6)$$

$$\frac{\partial N_n}{\partial t} - \frac{N_n U_n}{L} = -N_i N_n \xi_{ion}, \quad (7)$$

where N and U are the number density and mean velocity, and subscripts i and n denote ions and neutral atoms, respectively. To study the linear perturbation, a quantity follows the form: $Q = Q_0 + Q' \exp(-i\omega t)$, where Q_0 and Q' are equilibrium and perturbation quantities, respectively. From the first-order perturbation equation, the harmonic oscillator frequency can be given by

$$\omega = (N_{n,0} N_{i,0} \xi_{ion}^2)^{1/2}. \quad (8)$$

Using the zeroth-order equilibrium condition, one also obtains

$$\omega = \frac{(U_i U_n)^{1/2}}{L}, \quad (9)$$

where $U_i = (eV_D/M_i)^{1/2}$ is a function of the discharge voltage V_D. Although ionization oscillations depend on other parameters such as the mass flow rate, magnetic field topology, and channel wall material, it is assumed that these are incorporated into the ionization length L.

Figure 7 shows the time dependent results of the predator-prey model for two different initial conditions. For the equilibrium quantities, $N_{n0} = 1 \times 10^{19}$ m^{-3} and $N_{i0} = 1 \times 10^{17}$ m^{-3} are considered. The ionization rate coefficient is assumed to be $\xi_{ion} = 2 \times 10^{-13}$ m^{-6}s^{-1}. The predator-prey model gives oscillations as long as the initial conditions differ from the equilibrium values. Thus, a perturbation in the ion density is prescribed in the figures.

In Fig. 7(a), the initial ion density is $1.5N_{i0}$ while the initial neutral atom density is N_{n0}. It can be seen that neutral atoms are initially consumed due to the excess in ion (electron) density. As the neutral atom density decreases, the ionization process weakens. The ion density (*predator*) increases again as the neutral atoms (*prey*) repopulate. The initial density perturbation is not too large so that the evolution of the predator and prey follows a sinusoidal. It can be seen from Fig. 7 that $N_i \sim \cos(t)$ while $N_n \sim -\sin(t)$. Thus, there is a 90 degree phase shift. The frequency from Eq. (9) is 31.8 kHz, or $\omega = 2 \times 10^6$ rad/s, which agrees with the frequency obtained from Fig. 7(a).

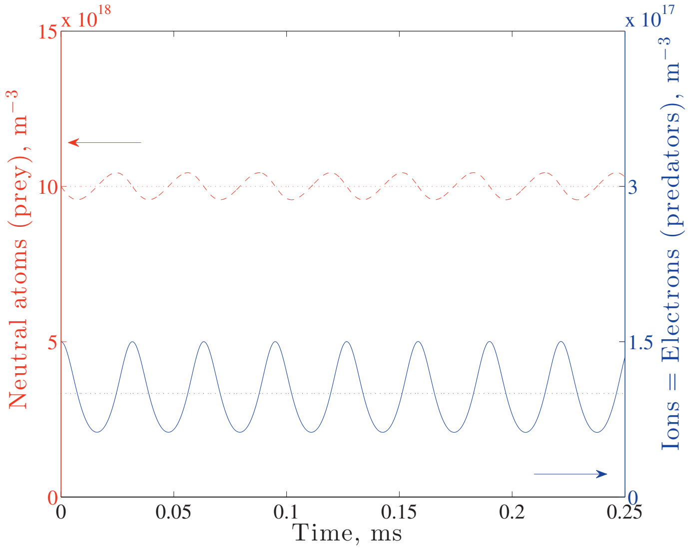

(a) Sinusoidal oscillation: Initial ion density is $1.5N_{i0}$

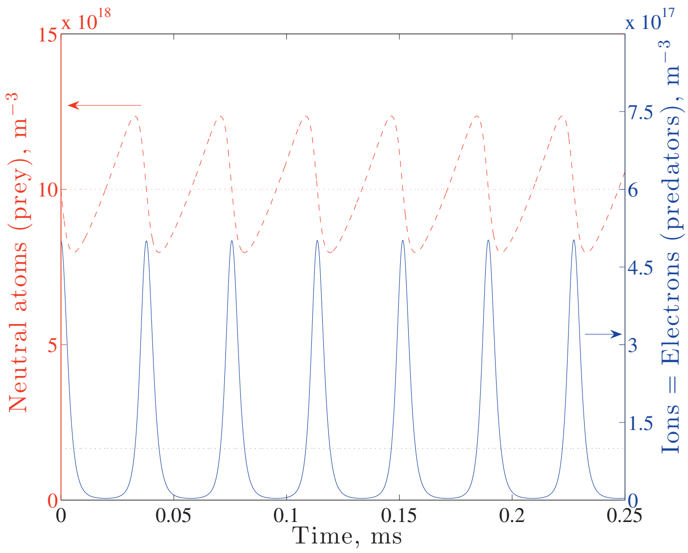

(b) Nonsinusoidal oscillation: Initial ion density is $5N_{i0}$

Figure 7. Lotka-Volterra model: Initial neutral atom density is $N_{n0} = 10^{19}$ m^{-3}. $N_{i0} = 10^{17}$m^{-3}.

In Fig. 7(b), the initial ion density is $5N_{i0}$, so the initial deviation from the equilibrium density is larger than Fig. 7(a). Neutral atoms are consumed and the ion density decreases quickly. The major difference from the small initial perturbation case is that the time evolution of ion and neutral atom densities is non-sinusoidal. The non-sinusoidal discharge oscillation is identified as a *nonlinear* mode in comparison to the small perturbation case that yields sinusoidal discharge oscillations is as a *linear* mode in Ref. 4. The frequency obtained from the numerical integration is 27.3 kHz, as there are only 6 periods during 0.22 ms. This disagrees with Eq. (9), which is obtained by assuming a linear perturbation $\exp(-i\omega t)$. It can be considered that in a strongly perturbed case, the evolution is no longer linear, thus higher order perturbation quantities, *nonlinear* effects, must be included.

Although the predator-prey model may capture some of the discharge and plasma oscillations in HETs, there are a few problems in the model.

1. The source of the oscillation is solely due to the discrepancy of the initial condition from the equilibrium values. The predator-prey model cannot describe the instability of the discharge oscillations.
2. The neutral inflow rate in the actual HET operation is fixed at the anode and the outflow varies, so Eq. (7) is inaccurate. The meaning of Eq. (7) is simply to satisfy the predator-prey model.
3. The ionization length, L, is not well-defined and is often assumed to be on the order of the channel length.

Therefore, a more complete model must be considered to study the mechanism of the ionization oscillation.

B. Flowing plasma discharge model

A 0D (zero-dimensional) model is useful to investigate the time evolution of a spatially-averaged quantity, which may not capture all of the detailed physics but provides a low order estimate.

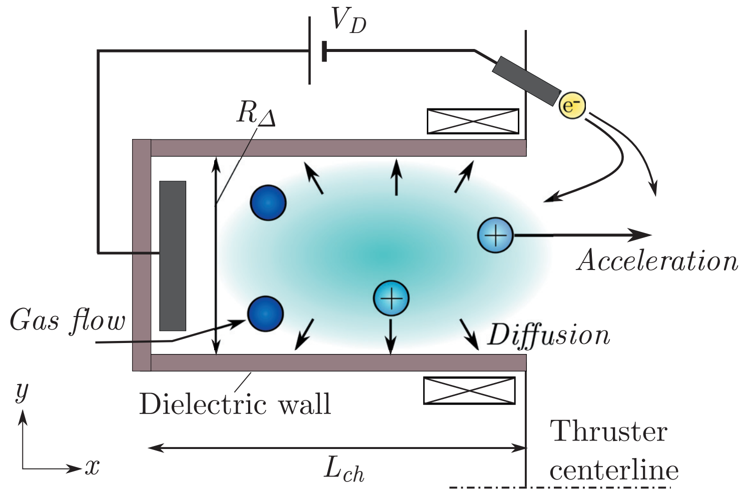

Figure 8. Schematic of the Hall thruster discharge region.

In order to construct a more accurate theory of ionization oscillations, the geometry is defined first. Figure 8 shows a simplified HET schematic used in the present model. The discharge plasma is assumed to be confined inside the discharge channel. Although the one-dimensional flow in the axial direction is of interest, the radial plasma diffusion also plays an important role. One can take an approach similar to a finite-volume method in which the state variables are volume averaged and the fluxes at interfaces are modeled. Without employing the undefined ionization length, ion and neutral continuity equations are more correctly given by

$$\frac{\partial N_i}{\partial t} + \frac{N_i U_i}{L_{ch}} + \frac{2 N_i U_{i,w}}{R_\Delta} = N_i N_n \xi_{ion} \tag{10}$$

$$\frac{\partial N_n}{\partial t} + \frac{(N_n - N_{int}) U_n}{L_{ch}} = -N_i N_n \xi_{ion}, \tag{11}$$

where N_{int} is the number density of neutral atoms at the anode, $U_{i,w} = (eT_e/m_i)^{1/2}$ is the ion acoustic speed, L_{ch} is the channel length, and R_Δ is the channel width. Ion diffusion toward the channel walls is taken into account assuming that Bohm's condition is satisfied at the sheath edge near the channel walls. Any spatial variations are neglected inside the box due to the 0D assumption. Since there is no radial diffusion for the neutral atoms, their transport can be described only by accounting for the axial transport.

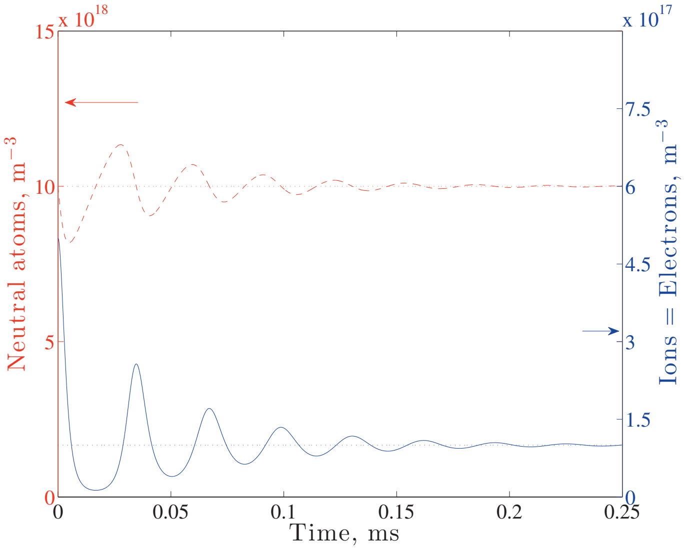

Figure 9. Heavy species transport model with constant ionization rate. Similar condition as Fig. 7(b): Initial ion density is 5 N_{i0}, but $N_{int} = 2 \times 10^{19}$ m^{-3} is also used.

A condition for a steady-state discharge plasma can be obtained as

$$\underbrace{N_{int}\xi_{ion}}_{\text{Maximum ion production}} > \underbrace{\frac{U_i}{L}}_{\text{Ion acceleration}}, \tag{12}$$

where the left hand side is the ionization frequency when ionizing all the inflow neutral gas and the right hand side is the characteristic frequency due to ion acceleration. For instance, the ionization rate needs to be sufficiently large to sustain a steady-state plasma when the ion outflow is fast. Given all the other parameters, the minimum T_e $(= T_{e,min})$ can be calculated when the two terms in Eq. (12) are equal. It can be seen from Eq. (12) that an increased U_i (via discharge voltage) or decreased N_{int} (via anode mass flow) increases $T_{e,min}$. Thus, the condition of having a steady-state plasma becomes more severe.

Figure 9 shows the heavy species transport model with a constant ionization rate. The equilibrium values are $N_{i0} = 1 \times 10^{17}$ m^{-3}, $N_{n0} = 1 \times 10^{19}$ m^{-3}, and $\xi_{ion} = 2 \times 10^{-13}$ m^{6}s^{-1}, which are the same as those employed for Fig. 7. The initial conditions are the same as Fig. 7(b), where a strong ionization oscillation is observed using the predator-prey model: $N_i = 5N_{i0}$ and $N_n = N_{n0}$. The inflow neutral atom density N_{int} is chosen to be $N_{int} = 2N_{n0} = 2 \times 10^{19}$ m^{-3}. It can be seen that the first oscillation cycle is similar to the predator-prey model. The large ion density yields a large ionization rate and the neutral atoms are consumed rapidly. The ion density also reaches a very small value. After one cycle, it can be already seen that the ionization oscillations start to dampen. This is due to the fixed neutral atom density at the inlet N_{int}. Then, the ion and neutral atom densities relax to the equilibrium values.

Damping of the ionization oscillation can be seen from the theoretical prediction. The first-order perturbation equations of Eq. (10) and (11) can be described as a system of equations

$$\begin{bmatrix} -i\omega & -N_{i,0}\xi_{ion} \\ \frac{U_i}{L} & -i\omega + \frac{N_{int}}{N_{int}-N_{n,0}} N_{i,0}\xi_{ion} \end{bmatrix} \cdot \vec{Q} = \mathbf{O} \tag{13}$$

for $\vec{Q} = [N_i', N_n']^T$. The frequency of the oscillations can be written as the real frequency and the growth rate as $\omega = \omega_r + i\gamma$, where ω_r and γ are always real numbers, assuming the perturbation to follow $\exp(-i\omega t)$.

The solution to Eq. (13) is given by

$$\omega_r = \pm\left(N_{i,0}N_{n,0}\xi_{ion}^2 - \gamma^2\right)^{\frac{1}{2}} \tag{14}$$

$$\gamma = -\frac{1}{2}\frac{N_{int}}{N_{int}-N_{n,0}}N_{i,0}\xi_{ion}. \tag{15}$$

Equation (15) shows that the growth rate of the oscillation is always negative, *i.e.* the imaginary part of the oscillation contributes as damping, since $N_{int} > N_{n,0}$ to have a steady-state plasma. Therefore, only solving the two continuity equations shows that the oscillation is always damped, *i.e.* $\gamma < 0$.

C. Forced ionization oscillation model

In order to investigate whether there is any oscillation induced due to the perturbation in the electron temperature, Eqs. (10) and (11) are solved with forced perturbation in the ionization rate. The simplified equations can be written as

$$\frac{\partial N_i}{\partial t} + \frac{N_i U_i}{L} = N_i N_n \xi_{ion}[1 + \Xi\cos(\omega_{r0}t)] \tag{16}$$

$$\frac{\partial N_n}{\partial t} + \frac{(N_n - N_{int})U_n}{L} = -N_i N_n \xi_{ion}[1 + \Xi\cos(\omega_{r0}t)], \tag{17}$$

where Ξ is the magnitude of ionization rate perturbation and ω_{r0} is the prescribed oscillation frequency. The values assumed are $N_{int} = 2N_{n0} = 2\times10^{19}$ m^{-3}, $N_i = 2N_{i0}$, $N_n = N_{n0}$, and $\omega_{r0} = 2\times10^5$ s^{-1}. The perturbations of ionization rate are chosen to be $\Xi = 1\times10^{-3}$, 0.01, and 0.05.

In Fig. 10(a), the ionization oscillations are damped for $\Xi = 1\times10^{-3}$. The neutral atom density of the inlet is fixed and damps the ionization oscillations that occur due to the initial conditions. It can be considered that the ionization oscillations are essentially damped although not completely damped due to a finite Ξ.

Figure 10(b) shows the ionization oscillations for a moderate perturbation of the ionization rate, $\Xi = 0.01$. The results look very similar to Fig. 7(a), in which a small perturbation is allowed in the predator-prey model. Sinusoidal oscillations are observed for both the ion and neutral atom densities. The magnitude of the ionization oscillations is approximately 50 %, which is significantly larger than the prescribed ionization perturbation rate, $\Xi = 0.01 = 1$ %. The most striking result of Fig. 10(b) is that the ionization oscillations can be excited with a small perturbation in the ionization rate, or equivalently the electron temperature.

Figure 10(c) shows the ionization oscillations for a strong perturbation of the ionization rate, $\Xi = 0.05$. The results look very similar to Fig. 7(b), in which a strong perturbation is prescribed for the initial condition. It can be seen that the oscillations grow in the first few cycles. In addition, the ion and neutral atom densities oscillate in a non-sinusoidal manner. The magnitude of the ionization oscillations exceeds that of the initial perturbation. Although the electron energy perturbation is not solved for in this analysis, the non-sinusoidal oscillations are likely to occur when the growth rate is large for the perturbation theory.

V. Complete perturbation theory including Ion Momentum and Electron Energy Equations

It is shown from Eqs. (14) and (15) that ionization oscillations always damp when there is no perturbation in the ionization rate coefficient ξ_{ion}, or equivalently the electron temperature T_e. However, the oscillations can grow linearly when there is moderate perturbation in the electron temperature. In order to investigate the source of such oscillations, we further extend the theory to include ion momentum and electron energy equations.

A. Formulation

In addition to the continuity equations for ions and neutral atoms, the perturbations in ion momentum and electron temperature are now taken into consideration. The ion momentum equation in the axial direction is given by

$$\frac{\partial}{\partial t}(N_i U_i) + \frac{N_i U_i^2}{L} = \frac{e}{M_i}N_i E, \tag{18}$$

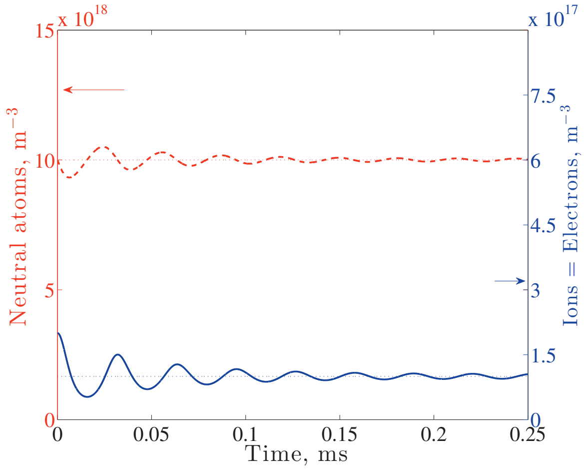

(a) Perturbation rate 0.1 %: Damped

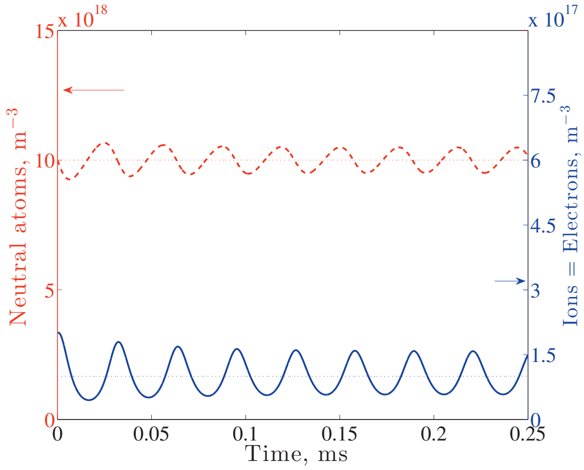

(b) Perturbation rate 1 %: Linear

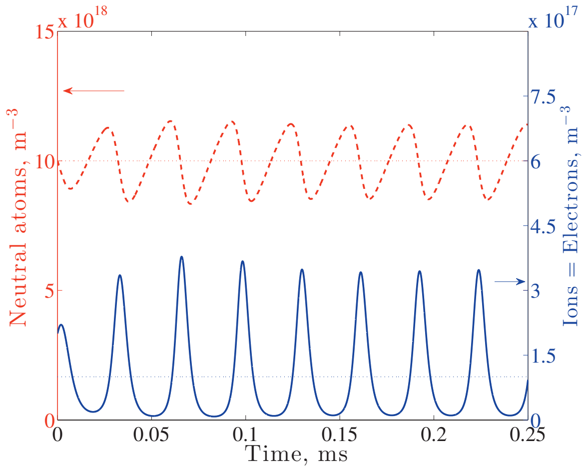

(c) Perturbation rate 5 %: Nonlinear (linear growth)

Figure 10. Heavy species transport model with perturbation of ionization rate.

where E is the electric field. The pressure term is neglected since the ions are assumed to be cold, *i.e.* $T_i \approx 0$. Next, the electron energy equation is taken into consideration.

$$\frac{\partial}{\partial t}\left(\frac{3}{2}N_e T_e\right) + \frac{5}{2}\frac{N_e U_e T_e}{L} = S_{joule} - S_{wall} - S_{coll}, \tag{19}$$

where $S_{joule} = -N_e U_e E$ is the energy gain due to Joule heating, $S_{wall} = N_e \epsilon_w(T_e)\nu_w(T_e)$ is the energy loss due to the channel walls, and $S_{coll} = \sum_j N_e N_n \xi_j(T_e)\epsilon_j$ denotes inelastic collisions, j, that contribute to energy loss. For simplicity, the contributions from electron pressure and heat conductivity are neglected. The convective energy flux at the exit is carried into the system since the electron velocity U_e is negative in HETs and it is assumed that the electron energy is sufficiently low at the anode so that there is no convective flux towards the anode. Finally, a quasineutral assumption is used, $N_i = N_e$. The details of the model are described in Ref. 12.

The perturbation equations for $\vec{Q} = [N_i', N_n', U_i', T_e']^T$ can be written as

$$\begin{bmatrix} -i\omega & -N_{i,0}\xi_{ion} & \frac{N_{i,0}}{L} & -N_{i,0}\frac{U_{i,0}}{L}\frac{\kappa}{T_{e,0}} \\ \frac{U_i}{L} & -i\omega + \frac{N_{int}}{N_{int}-N_{n,0}}N_{i,0}\xi_{ion} & 0 & N_{i,0}\frac{U_{i,0}}{L}\frac{\kappa}{T_{e,0}} \\ -i\omega U_{i,0} & 0 & N_{i,0}\left(-i\omega + \frac{2U_{i,0}}{L}\right) & 0 \\ -i\omega\frac{3}{2}T_{e,0} & N_{i,0}\xi_{ion}\chi\epsilon_{ion} & 0 & N_{i,0}\left(-i\frac{3}{2}\omega + \Lambda\right) \end{bmatrix} \cdot \vec{Q} = \mathbf{O}, \tag{20}$$

where $N_{i,0} > 0$ to have a steady-state plasma, and Λ is the effective electron energy relaxation frequency that has contributions from the energy loss mechanisms such as wall loss, inelastic collisions, and the convective energy flux.

In the present study, $T_{e,0}$ is taken as a parameter as well as U_e instead of the operational parameters such as B and V_D. The determinant of Eq. (20) can be written as

$$-\omega^4 + i\omega^3 F_1 + \omega^2 F_2 + i\omega F_3 + F_4 = 0, \tag{21}$$

where the coefficients F_k $(k = 1, 2, 3, 4)$ are functions of the plasma parameters. Since it is difficult to derive the solutions analytically, we analyze the stability criteria using representative values of the flow in a SPT-100 thruster in the next section.

The nominal conditions are $N_{int} = 1.6 \times 10^{19}$ m^{-3} and $V_D = 300$ V. In order to investigate the stability of ionization oscillations in the SPT-100 thruster, U_e is varied from 0 to $-U_i$ and T_e is varied from $T_{e,min}$ to 25 eV. The expression for the ionization rate coefficient ξ_{ion} of ground-state xenon atoms proposed by Goebel and Katz[17] is used

$$\xi_{ion} \approx [AT_e^2 + B\exp(-C/T_e)]\left(\frac{8eT_e}{\pi m}\right)^{1/2}, \tag{22}$$

B. Comparison with Experiments

Here, the results from the perturbation theory are compared with Ref. 14 and some discussions are made for the observations in Ref. 6.

Sekerak[14] observed that the range of magnetic field strength for a stable discharge operation mode becomes narrower as the discharge voltage is increased as well as the anode mass flow rate, as shown in Fig. 11. For a given magnetic field strength, it can be seen that the discharge oscillation can be excited when increasing the discharge voltage and anode mass flow rate, particularly at $B_r/B_r^* = 0.5 - 0.7$.

Some aspects of the present theoretical framework can explain the experimental observations. Figure 12 illustrates the growth rate for three cases: (1) $[V_d, N_{int}] = [450$ V, 1.6×10^{19} m$^{-3}]$, (2) $[V_d, N_{int}] = [300$ V, 1.6×10^{19} m$^{-3}]$, and (3) $[V_d, N_{int}] = [300$ V, 2.2×10^{19} m$^{-3}]$,

First, an increased V_D yields a larger $T_{e,min}$ to obtain a steady-state plasma discharge. Thus, the condition for a steady-state discharge is more severe, *i.e.* narrower, than the baseline case in Fig. 12(b). In addition, even if the electron temperature stays constant when increasing V_D, the axial electron velocity $|U_e|$ is likely to increase. If the magnetic field strength is constant, the electric field increases, the $E \times B$ drift in the azimuthal direction increases, so $|U_e| \approx |(E/B)\Omega^{-1}|$ increases as well. Thus, the operation point is likely to shift down in Fig. 12(a), meaning that the growth rate can be larger compared to Fig. 12(b).

Second, the theoretical prediction for the larger anode mass flow rate case is shown in Fig. 12(c). Although $T_{e,min}$ decreases, *i.e.* the condition for a steady-state discharge plasma is larger, the instability

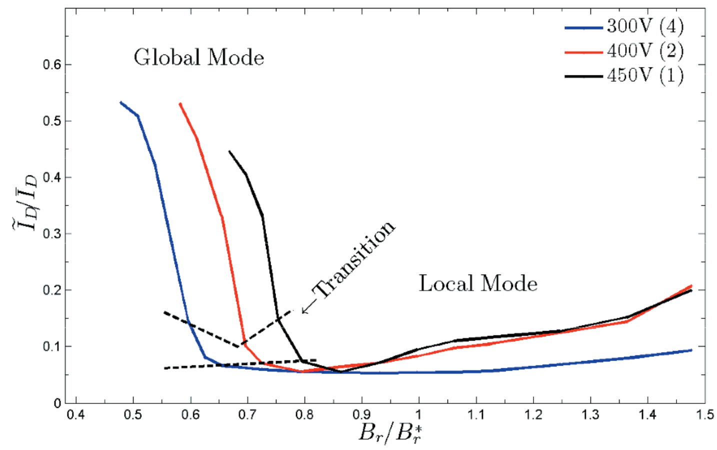

(a) Discharge voltage

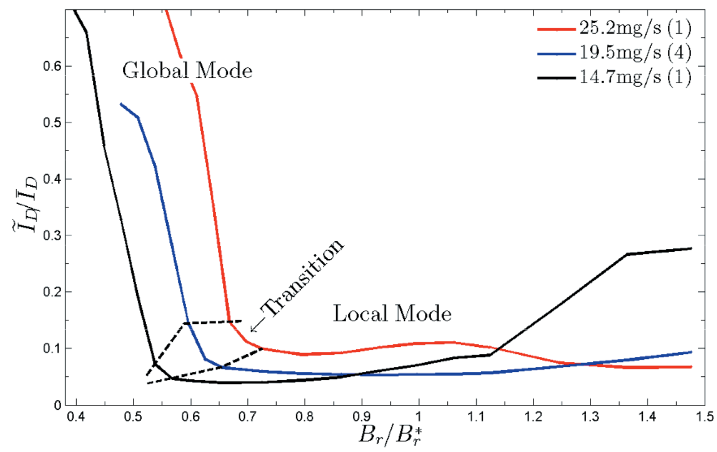

(b) Anode mass flow rate

Figure 11. Measurements of discharge current oscillation amplitudes in the H6 thruster. Reproduced from Figs. 4.2 and 4.3 of Ref. 14:

region, where $\gamma > 0$, is wider than Fig. 12(b). In addition, even when the operation point, U_e/U_i and T_{e0}, is kept the same when increasing N_{int}, the growth rate increases. For instance, at $(T_{e,0}, U_e/U_i) = (20$ eV, $-0.4)$, $\gamma = 3\times10^4$ rad/s in Fig. 12(c) whereas $\gamma = 1.2\times10^4$ rad/s in Fig. 12(b). These observations indicate that the stability condition is more severe for increased V_D and N_{int}, which agrees qualitatively with the experiments.

VI. Summary

A hybrid-DK simulation and a linear perturbation theory of the ionization instability are used to investigate the discharge oscillations in HETs. It is shown that the numerical results are in good agreement with experiments in terms of the discharge current oscillations and the breathing mode frequency. The numerical simulations indicate that electron transport is the key contributor to the stabilization of discharge oscillations. Particularly, the electron energy transfer between the Joule heating and other cooling mechanisms such as the convective heat flux and wall heat flux may determine the excitation and stabilization of the oscillations.

The perturbation theory that accounts for the ion and neutral continuity, ion momentum, and electron energy equations shows that perturbation in the electron energy is required for the ionization instability to occur. Otherwise, any oscillations can dampen due to the fixed neutral atom flow from the anode. Inclusion

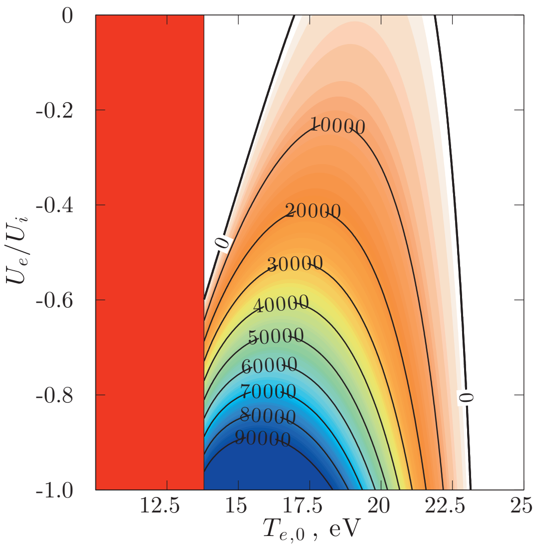

(a) $V_d = 450$ V, $N_{int} = 1.6 \times 10^{19}$ m^{-3}.

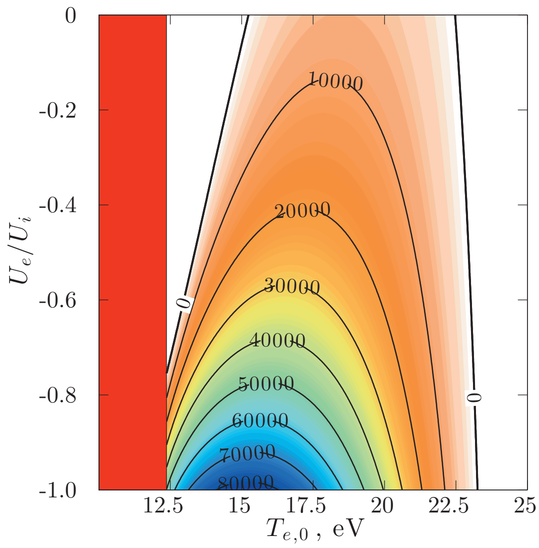

(b) $V_d = 300$ V, $N_{int} = 1.6 \times 10^{19}$ m^{-3}. **Baseline**

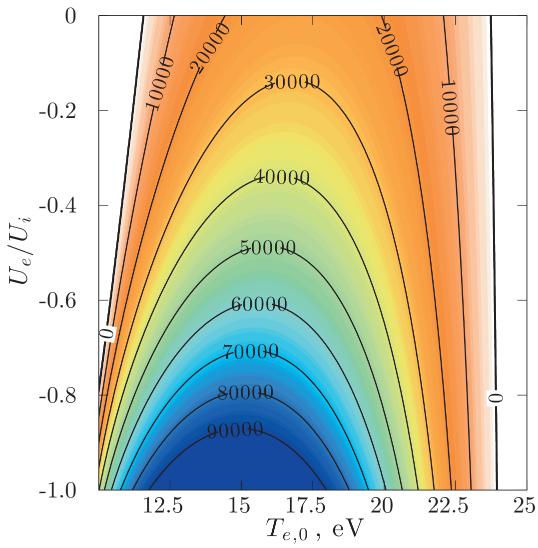

(c) $V_d = 300$ V, $N_{int} = 2.2 \times 10^{19}$ m^{-3}.

Figure 12. Growth rates for different conditions. Note that red region shows the unstable region due to $N_{i,0} < 0$ and white region shows the stable region.

of the electron energy perturbation allows an undamped solution for the linear perturbations of the ionization oscillation wave. The parameters discussed in the present model are U_e (or η_c) and T_e. In addition, the present theory suggests the stabilization mechanism of ionization oscillations. Reduced electron transport and increased electron temperature yields a transition from an undamped oscillation mode to a stabilized mode, which agrees with the observations from the hybrid-DK simulation.

Acknowledgement

The authors acknowledge the support for this work provided by the U.S. Department of Energy Office of Science, Fusion Energy Sciences Program, Grant DESC0001939, and the Air Force Research Laboratory through the Michigan/Air Force Center of Excellence in Electric Propulsion (MACEEP) grant number F9550-09-1-0695. The research was in collaboration with the Jet Propulsion Laboratory, California Institute of Technology, under a contract with the National Aeronautics and Space Administration.

References

[1]Boeuf, J. P. and Garrigues, L., "Low Frequency Oscillations in a Stationary Plasma Thruster," *Journal of Applied Physics*, Vol. 84, No. 7, 1998, pp. 3541–3554. doi:10.1063/1.368529.

[2]Fife, J. M., *Hybrid-PIC Modeling and Electrostatic Probe Survey of Hall Thrusters*, Ph.D. thesis, MIT, 1998.

[3]Barral, S., Makowski, K., Peradzynski, Z., Gascon, N., and Dudeck, M., "Wall material effects in stationary plasma thruster. II. Near-wall and in-wall conductivity," *Physics of Plasmas*, Vol. 10, No. 10, October 2003, pp. 4137–4152.

[4]Barral, S. and Ahedo, E., "Low-frequency model of breathing oscillations in Hall discharges," *Phys. Rev. E*, Vol. 79, Apr 2009, pp. 046401. doi:10.1103/PhysRevE.79.046401.

[5]Tilinin, G. N., "High-frequency plasma waves in a Hall accelerator with an extended acceleration zone," *Sov. Phys. Tech. Phys.*, Vol. 22, 1977, pp. 974–978.

[6]Gascon, N., Dudeck, M., and Barral, S., "Wall material effects in stationary plasma thrusters. I. Parametric studies of an SPT-100," *Physics of Plasmas*, Vol. 10, No. 10, 2003, pp. 4123–4136. doi:10.1063/1.1611880.

[7]Sekerak, M. J., Longmier, B. W., Gallimore, A. D., Brown, D. L., Hofer, R. R., and Polk, J. E., "Mode Transitions in Hall Effect Thrusters," AIAA 2013-4116, San Jose, CA, July 2013.

[8]Yamamoto, N., Komurasaki, K., and Arakawa, Y., "Discharge Current Oscillation in Hall Thrusters," *Journal of Propulsion and Power*, Vol. 21, No. 5, 2005, pp. 870–876.

[9]Hara, K., Sekerak, M. J., Boyd, I. D., and Gallimore, A. D., "Mode transition of a Hall thruster discharge plasma," *Journal of Applied Physics*, Vol. 115, No. 20, 2014. doi:10.1063/1.4879896.

[10]Hara, K., Boyd, I. D., and Kolobov, V. I., "One-dimensional hybrid-direct kinetic simulation of the discharge plasma in a Hall thruster," *Physics of Plasmas*, Vol. 19, No. 11, 2012. doi:10.1063/1.4768430.

[11]Hara, K. and Boyd, I. D., "Low Frequency Oscillation Analysis of a Hall Thruster Using a One-Dimensional Hybrid-Direct Kinetic Simulation," IEPC-2013-266, Washington D.C., October 2013.

[12]Hara, K., Sekerak, M. J., Boyd, I. D., and Gallimore, A. D., "Perturbation analysis of ionization oscillations in Hall effect thrusters," *Physics of Plasmas (1994-present)*, Vol. 21, No. 12, 2014. doi:10.1063/1.4903843.

[13]Bareilles, J., Hagelaar, G. J. M., Garrigues, L., Boniface, C., Boeuf, J. P., and Gascon, N., "Critical assessment of a two-dimensional hybrid Hall thruster model: Comparisons with experiments," *Physics of Plasmas*, Vol. 11, No. 6, June 2004, pp. 3035–3046.

[14]Sekerak, M. J., *Plasma Oscillations and Operational Modes in Hall Effect Thrusters*, Ph.D. thesis, University of Michigan, 2014.

[15]Barral, S. and Ahedo, E., "On the Origin of Low Frequency Oscillations in Hall Thrusters," *AIP Conference Proceedings*, Vol. 993, 2008, pp. 439–442.

[16]Lee, C. and Lieberman, M. A., "Global model of Ar, O2, Cl2, and Ar/O2 highdensity plasma discharges," *Journal of Vacuum Science and Technology A*, Vol. 13, No. 2, 1995, pp. 368–380. doi:10.1116/1.579366.

[17]Goebel, D. and Katz, I., *Fundamentals of Electric Propulsion: Ion and Hall Thrusters*, Wiley, 2008.